

Numerical Simulation of HgCdTe Based Simultaneous MWIR/LWIR Photodetector for Free Space Optical Communication

A.D.D. Dwivedi^{1,*}, A. Pranav⁴, Gaurav Gupta² and P. Chakrabarti³

¹*Groupe Nanoélectronique, Laboratoire IMS, CNRS - UMR 5218 Université de Bordeaux, 351 Cours de la Liberation - 33405 Talence Cedex, France*

²*Centre for Research in Microelectronics, Department of Electronics Engineering, IIT-BHU, Varanasi, India*

³*Motilal Nehru National Institute of Technology, Allahabad-211004, India*

⁴*Department of Electronics and Communication Engineering Graphic Era University, Dehradune, India*

Abstract: In this paper we report a theoretically simulated multilayer Hg_{1-x}Cd_xTe based heterojunction photodetector for dual band operation at temperature 78K. The detector is designed to operate at two strategic atmospheric windows in the MIR (3.8 μm) and in the LWIR (10.6 μm) region. The device has been modeled using closed form analytical formula and is also simulated using the device simulation software ATLAS from SILVACO® international. The device has been theoretically characterized in respect of energy band diagram, electric field profile, current voltage characteristics, spectral response and quantum efficiency. The detector is expected to find application in free space optical communication at 3.8 μm and at 10.6 μm .

Keywords: Photodetector, Numerical simulation, quantum efficiency, spectral response.

1. INTRODUCTION

The key component of an optical receiver is the photodetector which converts incoming optical signal to the corresponding electrical signal. For optical communication systems handling billions of bits of information, it is necessary that photodetector should have a very high speed. For successful implementation of high-speed optical communication systems it is necessary to develop suitable photodetectors. An extensive research work has been carried out worldwide over the past decades for exploring various semiconductor photodetectors. There are two basic mode of optical communication e.g. guided optical communication that uses optical fibers as the channel and the unguided optical communication that uses free space as the channel. The latter is also known as free space optical communication. In guided optical communication system, the fibers used for optical communication are primarily made of glass (silica) which offers low loss in the near infrared (NIR) region, typically 0.85 μm to 1.65 μm . As the loss of glass increases significantly in the longer wavelength region optical fiber communication has not been developed so far, for operation in this region. However, halide fibers have been reported to offer extremely low loss up to 12 μm wavelength region. It is therefore, expected that in

near future, it would be possible to develop optical fiber communication in the long wavelength region as well. Free space optical communication on the other hand has several atmospheric windows in the near infrared region as well as in the long wavelength region. The two specific atmospheric windows at 9.6 μm and 10.6 μm have drawn special attention of the researchers for free space optical communication and opened up the possibility of exploiting infrared atmospheric transparency windows for free space optical communication. The beam, containing billion of bits of information comprising a combination of internet messages, video images, radio signals or computer files, in free space optics (FSO) systems are transmitted by laser source focused on highly sensitive ultrafast photodetector receivers. Such ultrafast high sensitive receivers operating in the long wavelength (LWIR) region deploy photovoltaic detectors based on narrow bandgap semiconductors. These receivers are equipped with telescopic lenses able to collect the photon stream and transmit digital data. A number of photodetectors based on narrow bandgap semiconductors, have been developed over the past decades for optical communication applications in long wavelength infrared (LWIR) region. The most promising semiconductor alloys for use in LWIR region is HgCdTe (MCT) belonging to II-VI family. Hg_{1-x}Cd_xTe semiconductor material based photodetector is the best choice for long wavelength infrared (LWIR) applications

*Address correspondence to this author at the Groupe Nanoélectronique, Laboratoire IMS, CNRS - UMR 5218, Université de Bordeaux, 351 Cours de la Liberation - 33405 Talence Cedex, France; Tel: +33 753422024; Fax: +33556371545; E-mail: adddwivedi@gmail.com

due to flexibility in tailoring its bandgap. For fabrication of high-sensitivity detectors the bandgap of HgCdTe semiconductor material can be tailored over a wide infrared (from 2 μm to 30 μm) spectral range. Recent advances of backside illuminated HgCdTe heterojunction photodiodes have enabled a third generation of multispectral photodetection. In reference [1-40] and references therein various infrared photodetectors have been studied using various approaches.

Because of the complicated and expensive fabrication process, numerical simulation has become a critical tool for the development of Hg_{1-x}Cd_xTe band-gap engineering devices. The goal of this work is investigate the spectral responses of dual band photo detectors by numerical simulation using ATLAS device simulation software from Silvaco Inc. Specifically, the work will focus on the simulation of simultaneous MWIR-LMWI dual band detectors spectral response for the MWIR–LWIR spectral regions for free space optical communication at two strategic atmospheric attenuation windows 3.8 μm and 10.6 μm respectively. We present numerically simulated results like energy band diagram, doping profile, electric field profile of dual band detector, dark current, spectral response and quantum efficiency of the LWIR junction, MWIR junction and MWIR–LWIR dual band detector using Atlas simulation tool.

2. DEVICE STRUCTURE AND Hg_{1-x}CD_xTE MATERIAL MODEL

The numerical simulations presented in this work is based on the MWIR-LWIR back-illuminated dual band photodetector structure shown in Figure 1. This device is composed of two back to back Hg_{1-x}Cd_xTe p-n junctions with different energy gap supposed to be grown on a suitable substrate, such as CdTe, ZnCdTe or sapphire. Larger band gap material based diode absorbs MWIR radiation and smaller band gap material absorbs LWIR radiation. Wider band gap material acts as window for LWIR radiation. We employ an ATLAS simulation approach [22]. Continuity equations for electrons and holes and the Poisson's equations are solved on a finite element grid using the simulation tool Atlas from SILVACO® international [22]. A detailed discussion of each one of the important parameters and their numerical expressions as a function of the temperature and alloy composition is discussed in following section.

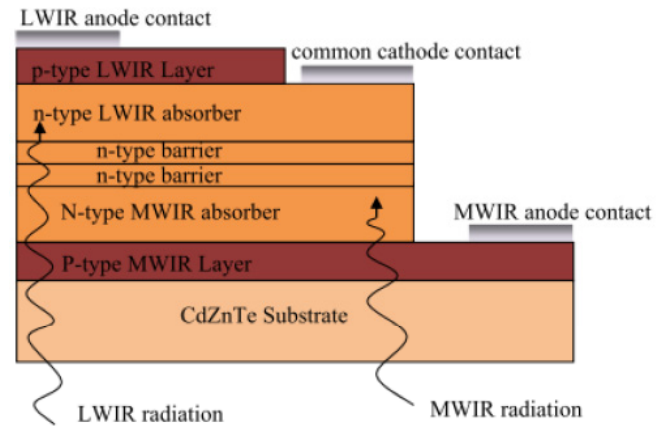


Figure 1: Device Structure.

The numerical computations have been carried out for theoretical characterization of Hg_{1-x}Cd_xTe based dual band detector for operation at temperature at 78 K. The mole fraction of cadmium in the ternary MCT material has been calculated so that the band gap energy of the material corresponds to the long wavelength cut-off value of 3.8 μm for MWIR and 10.6 μm for LWIR absorber layer. The band gap of Hg_{1-x}Cd_xTe as a function of temperature, T and alloy composition, x is included in the simulation model using the following empirical formula [23]

$$E_g = -0.302 + 1.93x - 0.810x^2 + 0.832x^3 + 5.35 \times 10^{-4} (1 - 2x) \left(\frac{-1822 + T^3}{255.2 + T^2} \right) \quad (1)$$

The intrinsic carrier concentration was calculated using the following expression [24]

$$n_i = \left(\begin{aligned} &5.24256 - 3.57290x - 4.74019 \times 10^{-4}T \\ &+ 1.25942 \times 10^{-2}xT - 5.77046x^2 - 4.24123 \times 10^{-6}T^2 \end{aligned} \right) \times 10^{14} E_g^{3/4} T^{3/2} \exp \left(\frac{-E_g}{2kT} \right) \quad (2)$$

where k is Boltzmann's constant. From Kane band Model the hole effective mass is taken as $m_p^* = 0.55 m_0$ and electron effective mass has been computed following [25] as

$$\frac{m_0}{m_n^*} = 1 + 2F + \frac{E_p}{3} \left(\frac{2}{E_g} + \frac{1}{E_g + \Delta} \right) \quad (3)$$

where $E_p = 19 \text{ eV}$, $F = -0.8$ and $\Delta = 1.0 \text{ eV}$.

The electron mobility has been computed using the empirical formula given by [23]

$$\mu_n = \frac{9 \times 10^4 s}{T^{2r}} \text{ m}^2/\text{Vs} \quad (4)$$

where $r = (0.2x)^{0.6}$ and $s = (0.2/x)^{7.5}$ which are valid in composition range $0.2 \leq x \leq 0.6$ and temperature range $T > 50\text{K}$.

The hole mobility has been assumed to be of the form [23]

$$\mu_h = \mu_0 \left[1 + \left(\frac{p}{1.8 \times 10^{23}} \right)^2 \right]^{-1/4} \quad (5)$$

where $\mu_0 = 0.044 \text{ m}^2/\text{Vs}$.

The absorption coefficient of $\text{Hg}_{1-x}\text{Cd}_x\text{Te}$ for optical carrier generation can be calculated within the Kane model, including the Moss-Burstein shift. For photon energy $E < E_g$ (tail region), $\alpha < \alpha_g$, the absorption coefficient obeys the rule [26-27]

$$\alpha = \alpha_0 \exp\left(\frac{\delta(E - E_0)}{kT}\right) \quad (6)$$

And for photon energy $E > E_g$ (Kane region), the absorption coefficient obeys the rule [27]

$$\alpha = \alpha_g \exp\left(\beta(E - E_g)\right)^{1/2} \quad (7)$$

where α_0 is the fitting parameter and

$$E_0 = -0.355 + 1.77x \quad (8)$$

$$\frac{\delta}{kT} = \frac{\ln \alpha_g - \ln \alpha_0}{E_g - E_0} \quad (9)$$

$$\alpha_g = -65 + 1.88T + (8694 - 10.315T)x \quad (10)$$

$$\beta = -1 + 0.083 + (21 - 0.13T)x \quad (11)$$

Modeling of Carrier Lifetime

For simulation of $\text{Hg}_{1-x}\text{Cd}_x\text{Te}$ based detectors the dominant recombination mechanisms include radiative recombination (direct band-to-band, and non-radiative

recombination mechanisms due to Auger process and Shockley-Read-Hall recombination. The radiative process takes place when free electron and hole recombine, emitting the excess energy in the form of a photon. The recombination rate for bands with spherical symmetry depends on the absorption coefficient through the equation [23]

$$G_R = \frac{8\pi}{h^3 c^3} \int_0^\infty \frac{\varepsilon(E) \alpha(E) E^2 dE}{\exp(E/kT) - 1} \quad (12)$$

where $\alpha(E)$ is the optical absorption coefficient, $\varepsilon(E)$ is relative dielectric constant, h is Planck's constant and c is speed of light. Ignoring the dispersion in dielectric constant and using the high frequency value of dielectric constant the radiative lifetime can be obtained as [23]

$$\tau_R = \frac{n_i^2}{G_R(n_0 + p_0)} \quad (13)$$

where n_i is intrinsic carrier concentration, n_0 and p_0 are the thermal equilibrium concentrations for electrons and holes respectively. The dependence of α on E as analyzed by Bardeen *et al.* can be expressed as [28]

$$\alpha(E) = \frac{2^{2/3} m_0 q^2}{3\varepsilon_\infty^{1/2} \hbar^2} \left(\frac{m_n^* m_p^*}{m_0(m_n^* + m_p^*)} \right)^{3/2} \left(1 + \frac{m_0}{m_n^*} + \frac{m_0}{m_p^*} \right) \left(\frac{E - E_g}{m_0 c^2} \right)^{1/2} \quad (14)$$

where E_g is material band gap, m_0 is free electron mass, m_n^* is the effective mass of electrons, m_p^* is the effective mass of holes, ε_∞ is high frequency dielectric constant, E_g is material bandgap in eV and $\hbar = h/2\pi$, h being the Planck's constant. Based on this expression and assuming $E_g > kT$ and neglecting the dispersion in the dielectric we can obtain G_R as [23]

$$G_R = 5.8 \times 10^{-13} n_i^2 \varepsilon_\infty^{1/2} \left(1 + \frac{m_0}{m_n^*} \right) \left(\frac{m_0}{m_n^* + m_h^*} \right)^{3/2} \times \left(\frac{300}{T} \right)^{3/2} \left(E_g^2 + 3kTE_g + 3.75k^2T^2 \right) \quad (15)$$

where k is Boltzmann constant, T is temperature and n_i is the intrinsic carrier concentration.

Shockley-Read Hall mechanism is not an intrinsic process, as it occurs via levels in the forbidden energy

gap. It may be reduced by lowering concentrations of native defects and foreign impurities. In the Shockley-Read mechanism, generation and recombination occurs via energy levels introduced by impurities or lattice defects into the forbidden energy gap. As recombination centers they trap electrons and holes; as generation centers, they successively emit them. The rates of generation and recombination depend on the individual nature of the center and its predominant occupation state of the charge carriers as well as on the local densities of those carriers in the bands of the semiconductor. The expression for the Shockley-Read lifetime in n-type material is given as [29]

$$\tau_{SRH} = \frac{1}{\sigma_p v_{th} N_f} \quad (16)$$

where, σ_p is capture cross section, N_f is trap density and the thermal velocity of charge carrier in n-type $Hg_{1-x}Cd_xTe$ alloy is given as

$$v_{th} = \sqrt{\frac{8kT}{\pi m_n^*}} \quad (17)$$

The band to band Auger effects are classified in several processes according to related bands. Beattie has determined ten types of photon-less Auger recombination mechanisms that are possible in a semiconductor with a single conduction band and heavy and light hole valence bands [23]. They have the smallest threshold ($E_f \approx E_g$) and the largest combined density of states. The CHCC recombination mechanism (Auger-1) involves two electrons and a heavy hole and is dominant in n type material. The CHLH process (Auger-7) is dominant in p-type material if the spin split-off band can be ignored. For materials such as $Hg_{1-x}Cd_xTe$ where the spin split-off energy Δ is much larger than the band gap energy E_g , the probability of the Auger transition through the conduction band/heavy-hole band/spin split-off band mechanism (called CHSH or Auger S) may be negligibly small in comparison with that of the CHLH Auger transition. Hence for narrow gap $Hg_{1-x}Cd_xTe$ only Auger-1 and Auger-7 need to be considered. The Auger lifetime (τ_{Aug}) is expressed as [23, 30]

$$\frac{1}{\tau_{Aug}} = \frac{1}{\tau_{A1}} + \frac{1}{\tau_{A7}} \quad (18)$$

where, τ_{A1} and τ_{A7} are lifetimes of carrier due to Auger-1 and Auger-7 transitions respectively, given as

$$\tau_{A1} = \frac{2\tau_{A1}^i}{1 + \left(\frac{n_0}{n_i}\right)^2} \quad (19)$$

$$\text{and } \tau_{A7} = \frac{2\tau_{A7}^i}{1 + \left(\frac{p_0}{n_i}\right)^2} \quad (20)$$

Here, τ_{A1}^i and τ_{A7}^i are the Auger-1 and Auger-7 lifetimes for intrinsic material [23]. The net carrier lifetime when effect of surface recombination is not taken into account is given as

$$\frac{1}{\tau} = \frac{1}{\tau_{SRH}} + \frac{1}{\tau_R} + \frac{1}{\tau_{Aug}} \quad (21)$$

3. SIMULATION PROCEDURE

The modeling procedure followed in this work is described here. The software used for this device modeling is a physically based, numerical device simulator from SILVACO called ATLAS. ATLAS is a physics-based, two dimensional device simulator that predicts the device's electrical behavior and enables the design of high performance semiconductor devices. It also provides significant insight into the mechanisms involved in device operation in that it can provide a two dimensional profile of carrier concentration, electric potential profiles, electric field lines and current density profiles. A complete documentation of ATLAS can be found in the available manual from Silvaco International [22]. The simulation procedure followed by the device simulation software, ATLAS, is presented in this section. The technique followed by this software is to solve a set of fundamental equations, which link the electrostatic potential and the carrier densities, numerically and in a holistic manner. The set of fundamental equations comprise of Poisson's equation, the continuity equations and the transport equations [41]. These are described as follows.

Poisson's Equation

Poisson's Equation relates variations in the electrostatic potential to local charge densities

It is mathematically described by the following relation

$$\nabla \cdot (\epsilon \nabla \psi) = -\rho \quad (22 a)$$

$$\nabla \cdot (\epsilon \nabla \psi) = -q(p - n + N_d^+ - N_a^-) \quad (22 b)$$

where ψ is the electrostatic potential, ρ is the local space charge density, ϵ is the local permittivity of the semiconductor (F/cm), p is the hole density (cm^{-3}), n is the electron density (cm^{-3}), N_d^+ is the ionized donor density (cm^{-3}) and N_a^- is the ionized acceptor density (cm^{-3}).

The reference potential is always taken as the intrinsic Fermi potential for simulations in ATLAS. The local space charge density is the sum of all contributions from all mobile and fixed charges, including electrons, holes and ionized impurities.

Continuity Equations

For electrons and holes, the continuity equations are defined as follows

$$\frac{\partial n}{\partial t} = \frac{1}{q} \nabla \cdot J_n + G_n - R_n \quad (23)$$

$$\frac{\partial p}{\partial t} = -\frac{1}{q} \nabla \cdot J_p + G_p - R_p \quad (24)$$

where n and p are the electron and hole concentrations, J_n and J_p are the electron and hole current densities, G_n (R_n) and G_p (R_p) are the generation (recombination) rates for the electrons and holes, respectively and q is the magnitude of the charge on the electron. ATLAS incorporates both eqns. in simulations, but, also gives the user an option to turn off one of the two equations and solve either the electron continuity equation.

Transport Equations

While equations (22)-(24) provide the general framework for device simulation, there are secondary equations that need to specify particular physical models for electron and hole current densities and generation (recombination) rates. The Current density equations are obtained by using the "drift-diffusion" charge transport model. The reason for this choice lies in the inherent simplicity and the limitation of the number of independent variables to just three, ψ , n and p . The accuracy of this model is excellent for all technologically feasible feature sizes. The drift-diffusion model is described as follows

$$J_n = qn\mu_n E_n + qD_n \nabla n \quad (25)$$

$$J_p = qp\mu_p E_p - qD_p \nabla p \quad (26)$$

where μ_n and μ_p are the electron and hole mobilities,

D_n and D_p are the electron and hole diffusion constants, E_n and E_p are the local electric fields for electrons and holes, respectively, and ∇n and ∇p are the three dimensional spatial gradient of n and p . The local electric fields are defined as follows

$$E_n = -\nabla(\psi + \frac{kT}{q} \ln n_{ie}) \quad (27)$$

$$E_p = -\nabla(\psi - \frac{kT}{q} \ln n_{ie}) \quad (28)$$

where n_{ie} is the local effective intrinsic carrier concentration. A key point here is that, ATLAS inherently assumes that the Einstein relationship holds good for the drift-diffusion model so that the diffusion constants and mobilities are proportional

$$D_n = \frac{kT}{q} \mu_n \quad (29)$$

$$D_p = \frac{kT}{q} \mu_p \quad (30)$$

The simulation procedure numerically and self-consistently solves the above equations and obtains electron and hole concentrations (n and p) and electrostatic potential (ψ) at all nodal points, biasing voltages, junction and contact lengths form the boundary conditions under which these equations are solved.

4. RESULTS AND DISCUSSIONS

In this section, a numerical simulation has been performed to the study the dual band detector structure shown in Figure 1. The device thickness along x direction is $40 \mu\text{m}$ and thickness of different layers along y direction is given in Table 1. The characteristics of the layers employed are presented in Table 1.

A program was developed separately for calculation of various characteristics of the photodetector using MATLAB platform by choosing appropriate material parameters. The simulated results were obtained by developing program in DECKBUILD window interfaced with ATLAS for multilayer heterojunction photodetector at 78K. Instead of the graded doping the numerical model includes a uniform doping profile. Once the physical structure of photodetector is built in ATLAS, the properties of the material used in device must be defined. A minimum set of data of material properties may include, bandgap, dielectric constant, electron affinity, densities of conduction and valance band

Table 1: Hg_{1-x}Cd_xTe Layer Thickness, Composition and Doping Employed in the MWIR-LWIR Dual Band Detector Structure

Layer	Thickness	Composition x	Doping (cm ⁻³)
P-type	9.0 μm	0.41	2.0×10 ¹⁷
N-type MW	6.25 μm	0.35275	5.0×10 ¹⁵
n-barrier	0.25 μm	0.345	5.0×10 ¹⁵
n-barrier	0.25 μm	0.345	1×10 ¹⁵
n-type LW	10.25 μm	0.2215	1×10 ¹⁵
p-type top	4.0 μm	0.31	2.0×10 ¹⁷

states, electron and hole mobility, optical recombination coefficient, and an optical file containing the wavelength dependent refractive index, *n* [22-42] and extinction coefficient, *K* [22-42] for the used materials.

The wavelength dependent values of extinction coefficient *K* is computed from the relation [22, 42]

$$K = \frac{\alpha\lambda}{4\pi} \tag{31}$$

The energy band diagram has been simulated from BLAZE, which is interfaced with ATLAS is a general purpose 2-D device simulator for III-V, II-VI materials, and devices with position dependent band structure (i.e., heterojunctions) [22]. BLAZE accounts for the effects of position dependent band structure by modifications to the charge transport equations. Energy band diagram for electron is shown in Figure 2 for the given device structure. In this diagram the layer thickness is given along x axis and conduction band and valance band energy are given along y direction. This energy band diagram corresponds to unbiased condition. Figure 3 shows doping profile of the dual band photodetector. Figure 4 shows electric field profile of the dual band detector at common cathode bias

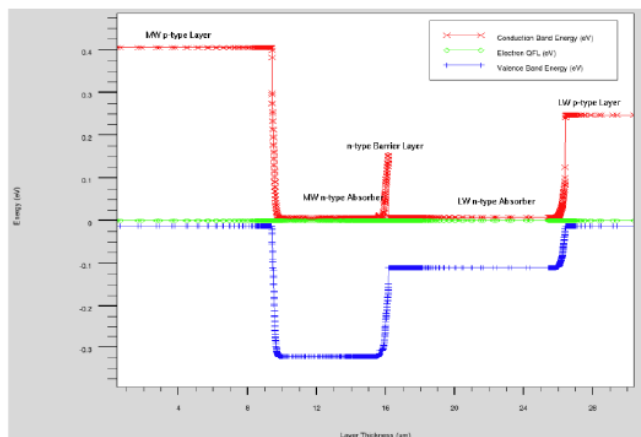


Figure 2: Energy band diagram of the dual band detector.

voltage of 2V. At this voltage the electric field is not so high to make the break down of any of the diodes MWIR and LWIR. Figure 5, Figure 6 and Figure 7 show forward and reverse bias I-V characteristic of LWIR, MWIR and MWIR-LWIR dual band detectors respectively in dark condition where current is plotted in log scale. It can be seen that dark currents of MWIR and LWIR detectors have been added up to give the dark current of MWIR-LWIR dual band detector.

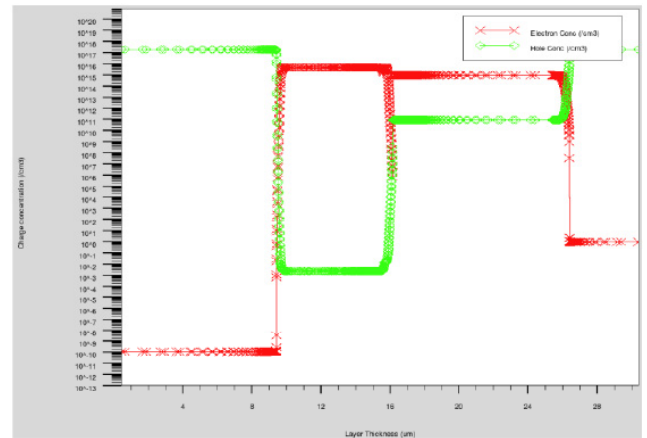


Figure 3: doping profile of the dual band detector.

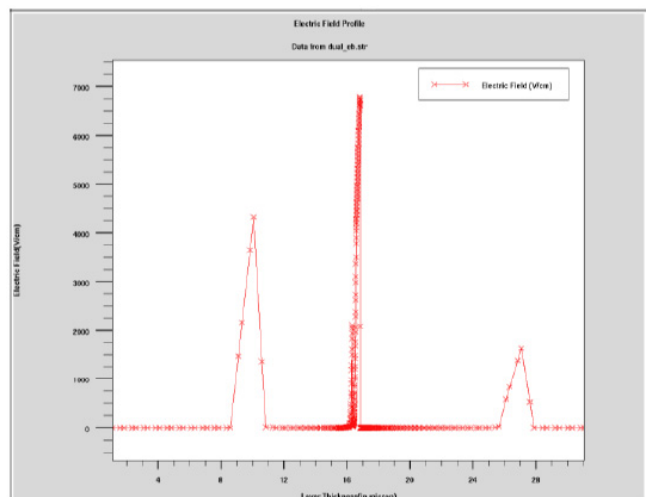


Figure 4: Electric field profile of the dual band detector.

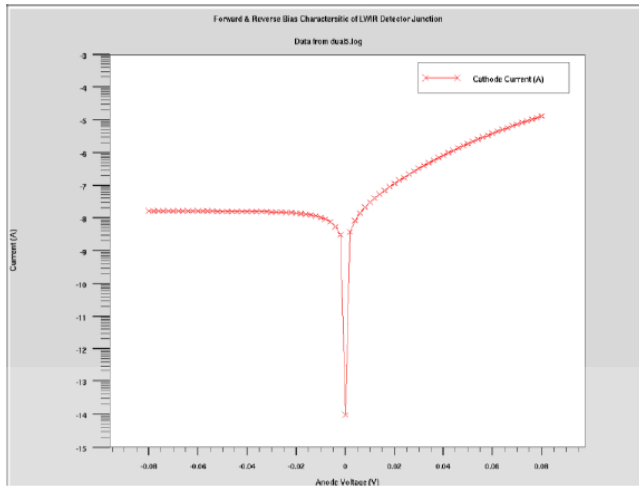


Figure 5: Forward and Reverse bias I-V characteristic of LWIR junction in dark condition.

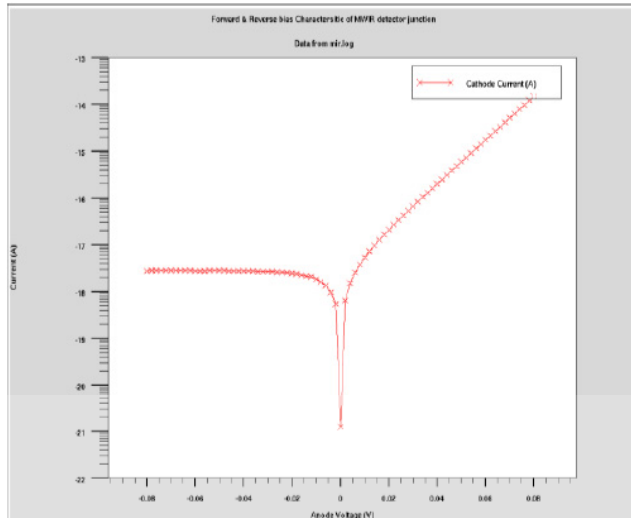


Figure 6: Forward and Reverse bias I-V characteristic of MWIR junction in dark condition.

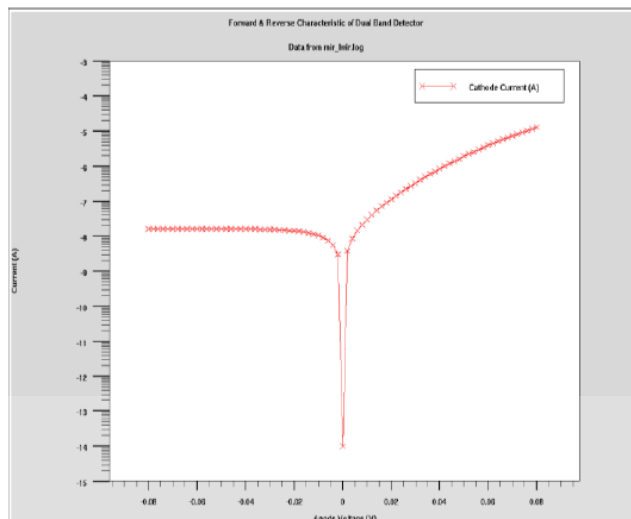


Figure 7: Forward and Reverse bias I-V characteristic of MWIR- LWIR dual band detector in dark condition.

The optical characteristics of the device have been studied by using LUMINOUS tool of ATLAS device simulator. The accurate modeling of electron hole pair generation is of primary importance in the simulation of photodetector. LUMINOUS, the optoelectronic simulation module in ATLAS, determines the photogeneration at each mesh point in an ATLAS structure by performing two simultaneous calculations. The refractive index n is used by LUMINOUS to perform an optical ray trace in the device. Difference in n values across the material boundaries determines the rate of light transmission and reflection. By following the path of light from the source to a mesh point, Luminous is able to determine the optical intensity at that point. Together, these simulations provide for wavelength dependent photogeneration throughout the photodetector [22, 42]. Figure 8 shows the calculated spectral response of MWIR-LWIR dual band detectors. In this figures three types of currents are given e.g. Source photocurrent, available photo current and cathode current as discussed in module LUMINOUS of TCAD Atlas Users' manual [22]. The spectral response, defined as device current as a function of wavelength of optical source.

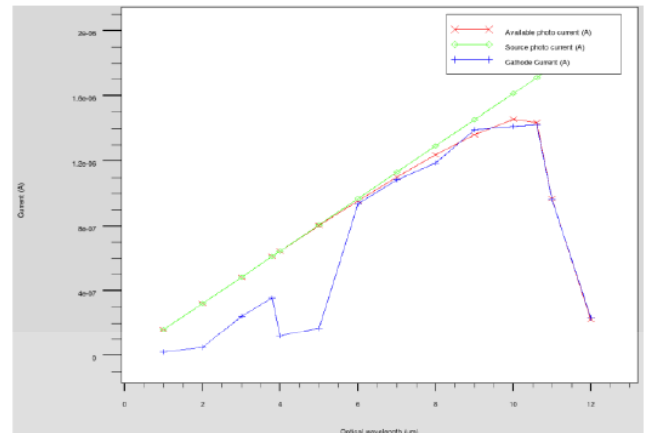


Figure 8: Spectral response of MWIR-LWIR dual band detector.

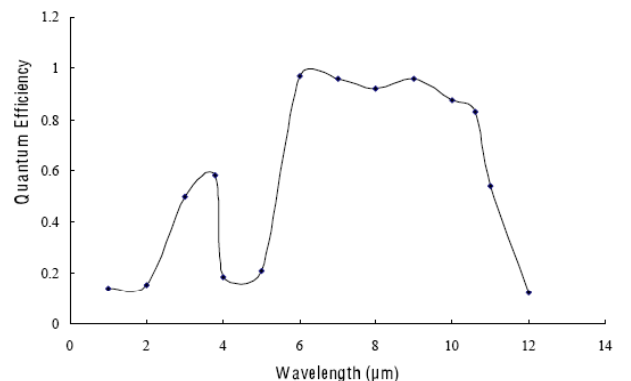


Figure 9: Quantum efficiency versus Wavelength (μm) of dual band detector.

External quantum efficiency is the ratio of cathode current to source photo current [22]. Figure 9 shows external quantum efficiency extracted from cathode current for MWIR-LWIR dual band detector. The dual band detector structure simulated in our case has nearly 90% and 60% external quantum efficiency in LWIR and MWIR spectral regions.

5. CONCLUSION

The simulated dual band detector structure can be operated at temperature 78 K and MWIR and LWIR longer wavelength cut off are 3.8 μm and 10.6 μm respectively. It would be very much attractive for free space optical communication in simultaneous dual band detection. Using these modeling and simulation guidelines one can also optimize the device for operation at different temperature and longer wavelength cut off. We have simulated for the above two longer wavelength cut off because there are two strategic atmospheric attenuation windows at 3.8 μm and 10.6 μm in MWIR and LWIR spectral regions at which highest transmission is possible as compared to other wavelengths in the above spectral regions.

REFERENCES

- [1] Rogalski A. "Infrared detectors: status and trend," *Progr. Quantum Electron* 2003; 27: pp. 59-210.
[http://dx.doi.org/10.1016/S0079-6727\(02\)00024-1](http://dx.doi.org/10.1016/S0079-6727(02)00024-1)
- [2] Bellotti E, Orsogna DD.: Numerical analysis of HgCdTe simultaneous two-color photovoltaic infrared detectors. *IEEE J. Quantum Electron* 2006; 42: 418-426.
<http://dx.doi.org/10.1109/JQE.2006.871555>
- [3] Reine M, Sood A, Tredwell T. "Photovoltaic infrared detector," in *Mercury Cadmium Telluride. ser. Semiconductors and Semimetals*, RK. Willardson and AC. Beer, Eds. New York: Academic 1981; 18: pp. 201-311.
- [4] Norton P. "HgCdTe infrared detectors," *Opt.-Electron. Rev.*, 2002; 10 no. 3: pp. 159-174.
- [5] Reine M. "Review of HgCdTe photodiodes for IR detection," in *Proc. SPIE Infrared Detectors Focal Plane Arrays*, vol. 4028, Orlando, FL Apr. 2000; pp. 320-330.
<http://dx.doi.org/10.1117/12.391745>
- [6] Reine M. "HgCdTe photodiodes for IR detection: a review," *Proc. SPIE Photodetectors Mater Dev VI Jan 2001*; 4288: pp. 266-277.
<http://dx.doi.org/10.1117/12.429413>
- [7] Tidrow M, Dyer W. "Infrared sensors for ballistic missile defense," *Infrared Phys. Technol* 2001; 42: pp. 333-336.
[http://dx.doi.org/10.1016/S1350-4495\(01\)00092-5](http://dx.doi.org/10.1016/S1350-4495(01)00092-5)
- [8] Reine M, Norton P, Star R, Weiler M, Kestigian M, Mitra P, et al. "Independently accessed back-to-back HgCdTe photodiodes: a new dual-band infrared detector," *J. Electron. Mater* 1995; 24 no. 5: pp. 669-679.
<http://dx.doi.org/10.1007/BF02657977>
- [9] Reine M, Hairston A, O'Dette P, Tobin S, Smith F, Musicant B, et al. "Simultaneous MW/LW dual-band MOVPE HgCdTe 64x64 FPAs," in *Proc. SPIE Infrared Detect. Focal Plane Arrays V Apr. 1998*; 3379: Orlando, FL, pp. 200-212.
- [10] Rajavel R, Jamba D, Jensen J, Wu OK, Brewer P, Wilson J, et al. "Molecular beam epitaxial growth and performance of HgCdTe-Based Simultaneous- Mode two-color detectors," *J Electron Mater* 1998; 10 no. 6: pp. 747-751.
<http://dx.doi.org/10.1007/s11664-998-0047-x>
- [11] Rajavel R, Jamba D, Jensen J, Wu OK, Wilson J, Johnson J, et al. "Molecular beam epitaxial growth and performance of integrated multispectral HgCdTe photodiodes for the detection of Mid-wave infrared radiation," *J Cryst Growth* 1998; 184: pp. 1272-1278.
[http://dx.doi.org/10.1016/S0022-0248\(97\)00811-7](http://dx.doi.org/10.1016/S0022-0248(97)00811-7)
- [12] Rajavel R, Jamba D, Wu OK, Jensen J, Wilson J, Patten E, et al. "High performance HgCdTe two-color infrared detector grown by molecular beam epitaxy," *J Cryst Growth* 1997; 175: pp. 653-658.
[http://dx.doi.org/10.1016/S0022-0248\(96\)01200-6](http://dx.doi.org/10.1016/S0022-0248(96)01200-6)
- [13] Kosai K. "Status and applications of HgCdTe device modeling," *J Electron Mater* 1995; vol. 24 no. 5: pp. 635-640.
<http://dx.doi.org/10.1007/BF02657972>
- [14] Robinson H. "Process modeling of HgCdTe infrared photodetectors," *J Electron Mater* 1998; 27 no. 6: pp. 589-594.
<http://dx.doi.org/10.1007/s11664-998-0020-8>
- [15] Williams G, De Wames R. "Numerical simulation of HgCdTe detector characteristics," *J Electron Mater* 1995; 24 no. 9: pp. 1239-1248.
<http://dx.doi.org/10.1007/BF02653080>
- [16] Dhar V, Gopal V. "Infrared detector performance in an area array," *Opt Eng* 2001; 40 no. 5: pp. 679-691.
<http://dx.doi.org/10.1117/1.1356706>
- [17] "Optimum diode geometry in a two-dimensional photovoltaic array," *Opt Eng* 2000; 39 no. 8: pp. 2022-2030.
<http://dx.doi.org/10.1117/1.1303763>
- [18] Dhar V, Bhan R, Ashokan A. "Effect of built-in electric field on crosstalk in focal plane arrays using HgCdTe epilayers," *Infrared Phys Technol* 1998; 39: pp. 353-367.
[http://dx.doi.org/10.1016/S1350-4495\(98\)00024-3](http://dx.doi.org/10.1016/S1350-4495(98)00024-3)
- [19] Wenus J, Rutkowski J, Rogalski A. "Two-Dimensional analysis of double layer heterojunction HgCdTe photodiodes," *IEEE Trans. Electron Dev Jul. 2001*; 48 no. 7: pp. 1326-1332.
<http://dx.doi.org/10.1109/16.930647>
- [20] Józ'wikowski K, Rogalski A. "Computer modeling of Dual-Band HgCdTe photovoltaic detectors," *J Appl Phys* 2001; 90 no. 3: pp. 1286-1291.
<http://dx.doi.org/10.1063/1.1380989>
- [21] Mitra P, Reine M. "MOVPE growth of HgCdTe for bandgap engineering of IR detectors arrays," in *Proc. SPIE Mater. Dev. IV, 3629, San Jose CA Jan 1999*; pp. 64-73.
- [22] TCAD Atlas User's Manual, SILVACO® international.
- [23] Rogalski A, Adamiec K, Rutkowski J. "Narrow-gap semiconductor photodiodes," SPIE Press, Bellingham, Wasington, USA, 2000.
- [24] Capper P. *Properties of Narrow Gap Cadmium-Based Compounds*, EMIS data reviews series, No. 10, INSPEC, The institution of Electrical Engineers, London, 1995
- [25] Weiler MH. "Magneto-optical properties of Hg_{1-x}Cd_xTe Alloys," in *Semiconductors and Semimetals*, edited by R.K. Willordson And A.C. Beer, Academic Press, New York, 1981; 16: pp 119-191.
- [26] Chu J, Mi Z, Tang D. "Band-to band absorption in narrow-gap Hg_{1-x}Cd_xTe semiconductors," *J Appl Phys* 1992; 71: pp. 3955-3961.
<http://dx.doi.org/10.1063/1.350867>
- [27] Chu J, li B, Liu K, Tang D. "Empirical rule of intrinsic absorption spectroscopy in Hg_{1-x}Cd_xTe," *J Appl Phys* 1994; 75: pp.1234-1235.
<http://dx.doi.org/10.1063/1.356464>
- [28] Bardeen J, Blatt FJ, Hall LH. " Indirect transitions from the

- valence to the conduction bands,"in Photoconductivity Conference, Atlantic city 1954; pp.146-154, edited by Breckenridge R, Russel B, Hahn E. Wiley, New York (1956).
- [29] Shockley W, Read WT. "Statistics of recombination of holes and electrons," Phys Rev 1952; 87: pp.835-842. <http://dx.doi.org/10.1103/PhysRev.87.835>
- [30] Pratt R, Hewett J, Jones PCC, Quelch M. "Minority carrier lifetime in n-type bridgman Hg Cd Te," J Appl Phys 1983; 54 no. 9: pp. 5152-5157. <http://dx.doi.org/10.1063/1.332739>
- [31] Dwivedi ADD. "Analytical Modeling and Numerical Simulation of P⁺-Hg_{0.69} Cd_{0.31}Te/n-Hg_{0.78}Cd_{0.22}Te/CdZnTe Heterojunction Photodetector for LWIR Free Space Optical Communication System," Journal of Applied Physics 2011; 110: 043101. <http://dx.doi.org/10.1063/1.3615967>
- [32] Dwivedi ADD. "Analytical Modeling and ATLAS Simulation of p⁺-Hg_{0.78} Cd_{0.22}Te/n-Hg_{0.78}Cd_{0.22}Te/CdZnTe Homo Junction Photodetector for LWIR Free Space Optical Communication System," Journal of Electron Devices 2011; 9: pp. 396-404.
- [33] Dwivedi ADD, Chakrabarti P. "Sensitivity Analysis of an Hg_{1-x}Cd_xTe based Photoconductive Receiver for Long Wavelength Free space optical communication at 9.6 μm," Journal of Electron Devices 2011; 9: pp. 390-395.
- [34] Dwivedi ADD, Mittal A, Agrawal A, Chakrabarti P. "Analytical Modeling and ATLAS Simulation of N⁺-InP/n⁰-In_{0.53}Ga_{0.47}As/p⁺In_{0.53}Ga_{0.47}As p-i-n Photodetector for Optical Fiber Communication," Infrared Physics & Technology 2010; 53 no. 4: p. 236-245. <http://dx.doi.org/10.1016/j.infrared.2010.03.003>
- [35] Dwivedi ADD, Chakrabarti P. "Analytical Modeling and ATLAS Simulation of N⁺-Hg_{0.69} Cd_{0.31}Te /n⁰- Hg_{0.78} Cd_{0.22}Te/p⁺Hg_{0.78} Cd_{0.22}Te p-i-n Photodetector for Long wavelength Free Space Optical Communication," Optoelectronics and Advanced Materials-Rapid Communications (OAM-RC) 2010; 4 no 4: pp. 480-497.
- [36] Dwivedi ADD. Arun Kumar Singh, Rajiv Prakash and P. Chakrabarti, "A Proposed Organic Schottky Barrier Photodetector for application in the Visible Region," Current Applied Physics 2010; 10: pp. 900-903. <http://dx.doi.org/10.1016/j.cap.2009.10.019>
- [37] Arun Kumar Singh, Dwivedi ADD, Chakrabarti P, Rajiv Prakash. "Electronic and Optical Properties of Electrochemically Polymerized Polycarbazole/Aluminum Schottky Diodes," Journal of Applied Physics 2009; 105: 114506. <http://dx.doi.org/10.1063/1.3139277>
- [38] Dwivedi ADD, Chakrabarti P. "Sensitivity analysis of an HgCdTe based photovoltaic receiver for long- wavelength free space optical communication systems" Optoelectronics Letters 5, pp. 21-25. <http://dx.doi.org/10.1007/s11801-009-8123-x>
- [39] Dwivedi ADD, Chakrabarti P. "Modeling and Analysis of Photoconductive Detectors based on Hg_{1-x}Cd_xTe for free Space Optical Communication." Optical and Quantum Electronics 2009; 39: pp. 627-641. <http://dx.doi.org/10.1007/s11082-007-9122-4>
- [40] Hu WD, Chen XS, Ye ZH, Lin C, Yin F, Lu W." Numerical analysis of two-color HgCdTe infrared photovoltaic heterostructure detector" Opt Quant Electron 2009; 41: 699-704. <http://dx.doi.org/10.1007/s11082-010-9381-3>
- [41] Dwivedi ADD. " Numerical Simulation and Spice Modeling of Organic Thin Film Transistors (OTFTs)" International Journal of Advanced Applied Physics Research 2014; 1 no. 2: 1421. <http://dx.doi.org/10.15379/2408-977X.2014.01.02.3>
- [42] Dwivedi ADD, Chakrabarti P. "Modeling and ATLAS simulation of HgCdTe based MWIR photodetector for free space optical communication," International Conference on Recent Advances in Microwave Theory and Applications (MICROWAVE-2008) 2008; pp.412 - 415. <http://dx.doi.org/10.1109/AMTA.2008.4763197>

Received on 27-04-2015

Accepted on 01-06-2015

Published on 15-06-2015

<http://dx.doi.org/10.15379/2408-977X.2015.02.01.5>

© 2015 Dwivedi *et al.*; Licensee Cosmos Scholars Publishing House.

This is an open access article licensed under the terms of the Creative Commons Attribution Non-Commercial License

(<http://creativecommons.org/licenses/by-nc/3.0/>), which permits unrestricted, non-commercial use, distribution and reproduction in any medium, provided the work is properly cited.